Porous Magneto-Fluorescent Superparticles by Rapid Emulsion Densification

Emanuele Marino,[1,2,†,*] Thi Vo,[3,4,†] Cristian Gonzalez,[1] Daniel J. Rosen,[5] Steven J. Neuhaus,[5] Alice Sciortino,[2] Harshit Bharti,[5] Austin W. Keller,[5] Cherie R. Kagan,[1,5,6] Marco Cannas,[2] Fabrizio Messina,[2] Sharon C. Glotzer,[3,7,*] Christopher B. Murray[1,5,*]

[1]Department of Chemistry, University of Pennsylvania, 231 S. 34th St., Philadelphia (PA), 19104 USA.

[2]Dipartimento di Fisica e Chimica, Università degli Studi di Palermo, Via Archirafi 36, 90123 Palermo, Italy.

[3]Department of Chemical Engineering, University of Michigan–Ann Arbor, Ann Arbor, Michigan 48109, USA.

[4]Department of Chemical and Biomolecular Engineering, Johns Hopkins University, Baltimore, Maryland 21218, United States

[5]Department of Materials Science and Engineering, University of Pennsylvania, 3231 Walnut St., Philadelphia (PA), 19104 USA.

[6]Department of Electrical and Systems Engineering, University of Pennsylvania, Philadelphia, PA, 19104, USA.

[7]Biointerfaces Institute, University of Michigan–Ann Arbor, Ann Arbor, Michigan 48109, USA.

Email: cbmurray@sas.upenn.edu, sglotzer@umich.edu, emanuele.marino@unipa.it

ABSTRACT: Porous superstructures are characterized by large surface area and efficient molecular transport. Although methods aimed at generating porous superstructures from nanocrystals exist, current state-of-the-art strategies are limited to single-component nanocrystal dispersions. More importantly, such processes afford little control over the size and shape of the pores. Here we present a new strategy for the nanofabrication of porous magneto-fluorescent nanocrystal superparticles that are well controlled in size and shape. We synthesize these composite superparticles by confining semiconductor and superparamagnetic nanocrystals within oil-in-water droplets generated using microfluidics. The rapid densification of these droplets yields spherical, monodisperse, and porous superparticles of nanocrystals. Molecular simulations reveal that the formation of pores throughout the superparticles is linked to repulsion between nanocrystals of different compositions, leading to their phase separation during self-assembly. We confirm the presence of nanocrystal phase separation at the single superparticle level by analyzing the changes in optical and photonic properties of the superstructures as a function of nanocrystal composition. This excellent agreement between experiments and simulations allows us to develop a theory that predicts superparticle porosity from experimentally tunable physical parameters such as nanocrystal size ratio, stoichiometry, and droplet densification rate. Our combined theoretical, computational, and experimental findings provide a blueprint for designing porous, multifunctional superparticles with immediate applications in catalytic, electrochemical, sensing, and cargo-delivery applications.

INTRODUCTION:

The field of nanoscale self-assembly has experienced tremendous growth over the last three decades, fueled by advances in the synthesis of complex nanocrystals (NCs) as well as increased control over their organization into complex superstructures. NCs can be assembled into amorphous,[1, 2] crystalline,[3-6] and quasicrystalline[7-9] superstructures (superlattices) by careful tuning of parameters such as NC shape,[10-19] stoichiometry,[20, 21] ligand design[22-24] and grafting density.[25-27] These experimental handles influence the magnitude[28, 29] and length scale[30, 31] of the emergent interparticle interactions between NCs that ultimately dictate the self-assembled morphologies. Currently, NC superlattices are the prime candidates for applications across a wide range of fields, including optoelectronic,[32, 33] catalytic,[34-36] and smart/adaptive materials.[37] However, achieving direct control over crystalline domain 1) size, 2) shape, and 3) density is currently an open challenge[38, 39] due to a lack of precision control over crystal growth. Specifically, unlike crystallization of atomic solids, nanoscale self-assembly protocols are performed in solution[3, 40] or at a liquid/air interface,[41, 42] prohibiting the use of physical templates to guide crystal propagation along a desired direction.

Along this vein, self-assembly in confinement represents a novel and promising route for templating nanofabrication. By forcing NCs to adhere to an *a priori* defined confinement geometry during the assembly process, increased precision can be obtained in the direction of crystal propagation and growth kinetics.[43] One popular approach employs the use of emulsion droplets to densify a dispersion of NCs. Radially symmetric shrinkage during densification creates geometrically defined set of walls that force NCs to organize into ordered, spherical superparticles, also known as supraparticles or supercrystals.[44-47] These superparticles are characterized by high density and low surface area, leading to strong light-matter interaction,

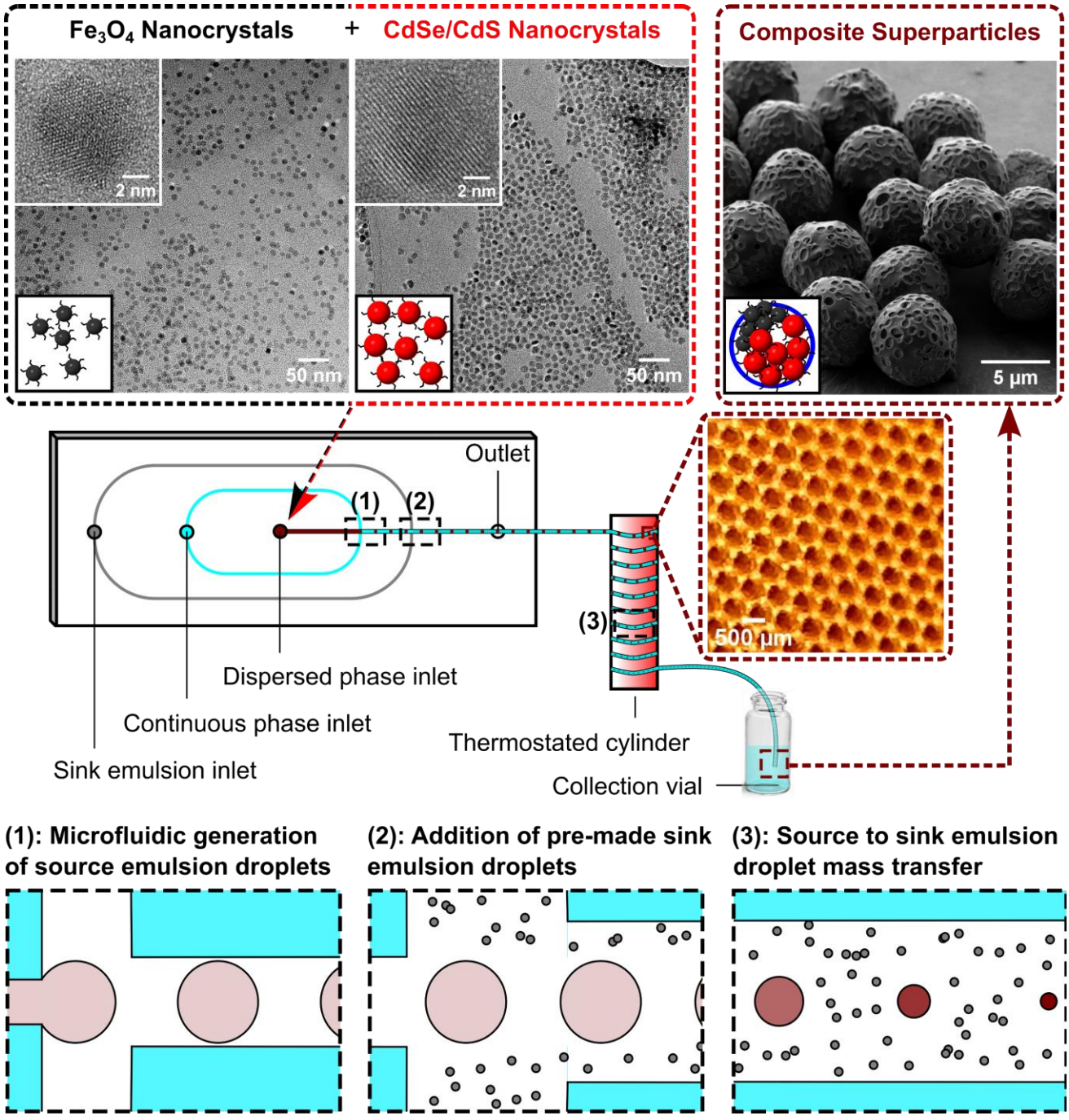

Figure 1: Generation of porous, monodisperse magneto-fluorescent superparticles from nanocrystal (NC) building blocks. Transmission electron micrographs of (top-left) superparamagnetic Fe_3O_4 NCs, depicted as black spheres, and (top-center) semiconductor CdSe/CdS NCs, depicted as red spheres. Insets show high-resolution micrographs of individual NCs. (Top-right) Scanning electron micrograph of magneto-fluorescent superparticles generated using the source-sink emulsion approach. (Bottom) Schematic of the source-sink emulsion approach facilitated by droplet microfluidics. First, monodisperse toluene-in-water droplets containing a dispersion of colloidal nanocrystals are generated (source droplets, **1**). Then the droplets are mixed with a hexadecane-in-water nanoemulsion (sink droplets, **2**). Finally, the transfer of toluene from source to sink droplets causes the formation of monodisperse superparticles (**3**).

making these artificial materials ideal candidates for applications in lasing,[48-50] stimuli-responsive materials and sensing,[37] and photonics.[51, 52]

These results suggest that emulsion templating has incredible potential in creating crystalline materials with well-defined sizes and shapes, two of the three constraints in superlattice engineering.

However, tuning superlattice densities remains elusive. While high density materials are optimal for light-matter interactions, low density (porous) superlattices are of interest in catalytic,[34-36] electrochemical,[53-55] sensing,[56, 57] and cargo uptake[58, 59] and release[59-61] applications. Conventional strategies for fabricating porous materials based on NCs include both top-down and

bottom-up methods. In top-down methods, exposure to an external stimulus introduces pores into an initially non-porous NC superstructure. This results in selective chemical etching of one NC type from a binary superlattice, leaving the final structure nanoporous.[62-64] For bottom-up methods, porous superstructures are a direct result of NC self-assembly, without the need for post-processing protocols.[65, 66] For instance, recently we succeeded in generating two-dimensional porous membranes through a strategy based on complementary ligands.[67] Such bottom-up methods work particularly well when using high aspect ratio, flexible NCs that cannot fill space efficiently, such as nanofibers,[68, 69] nanowires,[70, 71] or nanosheets.[72, 73] Nevertheless, controlling the size and shape of the porous domain represents a challenge due to a lack of precise control over the assembly kinetics.

Here, we extend the emulsion templating strategy to address the most elusive assembly constraint – tuning superlattice density. We present a protocol aimed at driving NC self-assembly into three-dimensional, porous, multicomponent, monodisperse superparticles. To do so, we confine a dispersion comprising two distinct NC types – Fe_3O_4 and CdSe/CdS – within the same droplet to drive their co-assembly upon droplet densification. The formation of multicomponent superparticles is accompanied by the emergence of structural voids previously unobserved in emulsion-based approaches. These microscale voids bridge the length scales of NCs (~10 nm) and superparticles (~10 μm), indicating the generalizability of artificial solids composed of NC superlattices towards cargo delivery and catalytic applications. We employ a combination of theory and simulation to elucidate the thermodynamic mechanism driving the formation of these porous morphologies, obtaining excellent agreement with experiment. Our results reveal a novel approach towards programmable porosity and hierarchical ordering within superparticles, highlighting the versatility of emulsion templating in multicomponent assemblies.

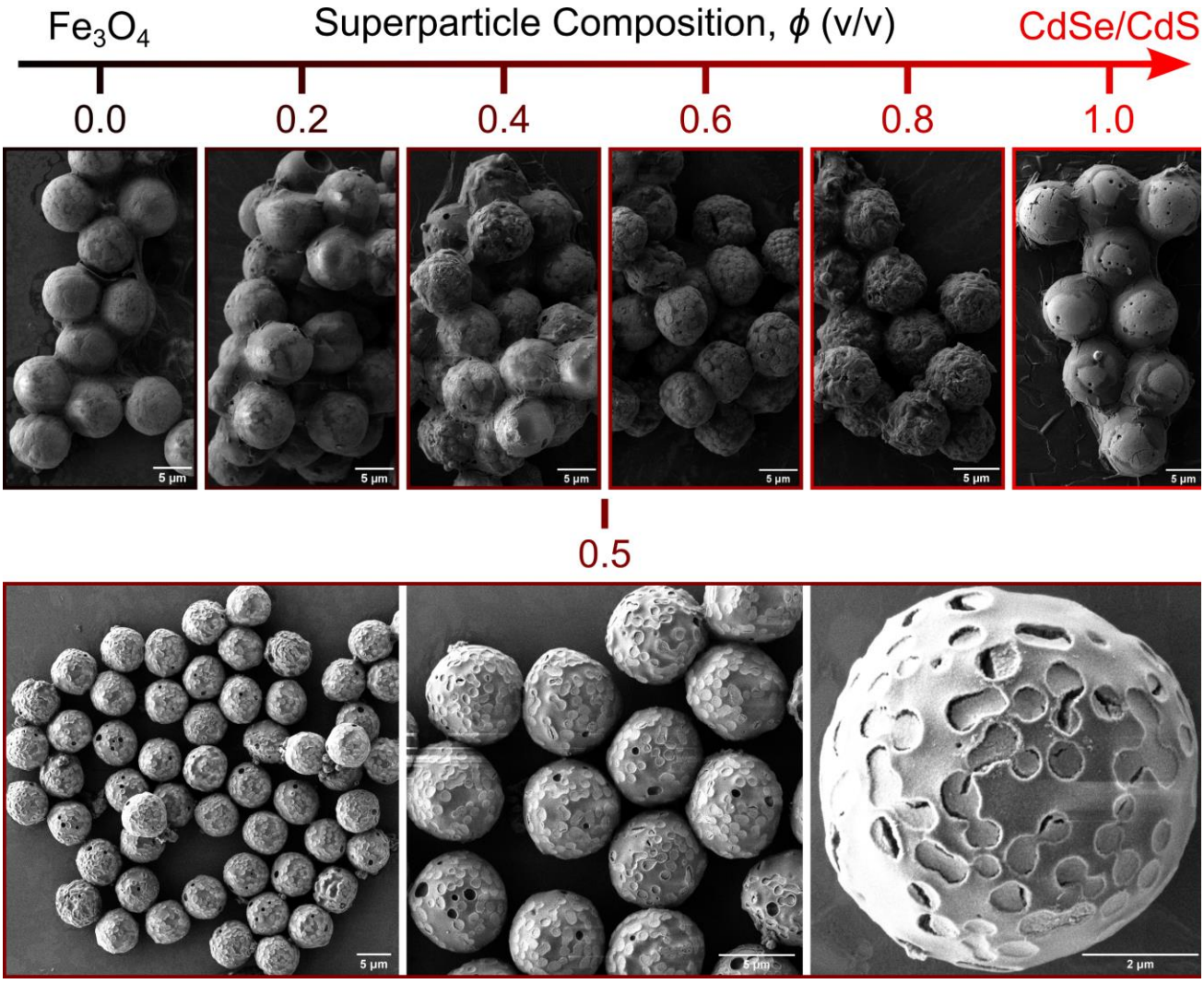

Figure 2: Composite superparticles reveal composition-dependent morphology. Scanning electron micrographs of magneto-fluorescent nanocrystal superparticles with compositions ranging from pure Fe_3O_4 ($\phi = 0$) to pure CdSe/CdS ($\phi = 1$), where ϕ is the fraction of semiconductor NCs. At intermediate compositions, the surface of the superparticles deviates from smooth, revealing circular depressions.

RESULTS AND DISCUSSION:

We synthesize Fe_3O_4 core and CdSe/CdS core/shell NCs stabilized by oleate ligands according to the literature.[74, 75] The transmission electron micrographs of the NCs dispersed on a carbon substrate are shown in the top left panels of **Figure 1**. The Fe_3O_4 NCs appear spherical, with a diameter of 9.2 nm ± 10 %, extracted through image analysis. CdSe/CdS NCs appear faceted, likely because of the slow, epitaxial growth of the CdS shell on the CdSe core. Their Feret diameter[76] is 13.1 nm ± 22 %, where the different orientations of the faceted NCs with respect to the electron beam likely contribute to their apparent higher size polydispersity.[77]

We combine these two types of NCs into superparticles by using our recently-developed source-sink emulsion templated assembly procedure.[48] Specifically, we use droplet microfluidics to prepare a monodisperse emulsion of toluene-in-water, the *source emulsion*, containing the binary dispersion of NCs at a total volume fraction of 0.01 %, volumetric ratio of the two NC types of 1:1 or $\phi = 0.5$, and NC size ratio $\gamma = 0.70$. The source emulsion is then mixed with a 55 nm hexadecane-in-water emulsion, or *sink emulsion*, that is prepared separately by extended tip sonication. The difference in aqueous solubility and internal pressure between source and sink droplets causes the spontaneous, unidirectional mass transfer of toluene from the source to the sink emulsion. This results in the rapid densification of the monodisperse source droplets to yield monodisperse NC superparticles with a diameter of 6.6 μm ± 4 %, as shown in the scanning electron micrographs in the top right panel of **Figure 1**. The NC superparticles are well-dispersed, as shown graphically in Figure S2 and quantitatively in our previous contribution.[48] A schematic of the assembly procedure is shown in the bottom panel of **Figure 1**, while further details are provided in the Materials and Methods section and in the recent literature.[48, 50, 52]

The NC superparticles show surface depressions with circular cross-sections of approximately 0.48 μm in radius. Some depressions appear to have merged to form dipolar shapes, while others are larger and lead to an empty volume within the superparticle. We explore the appearance of these surface characteristics by preparing NC superparticles with different

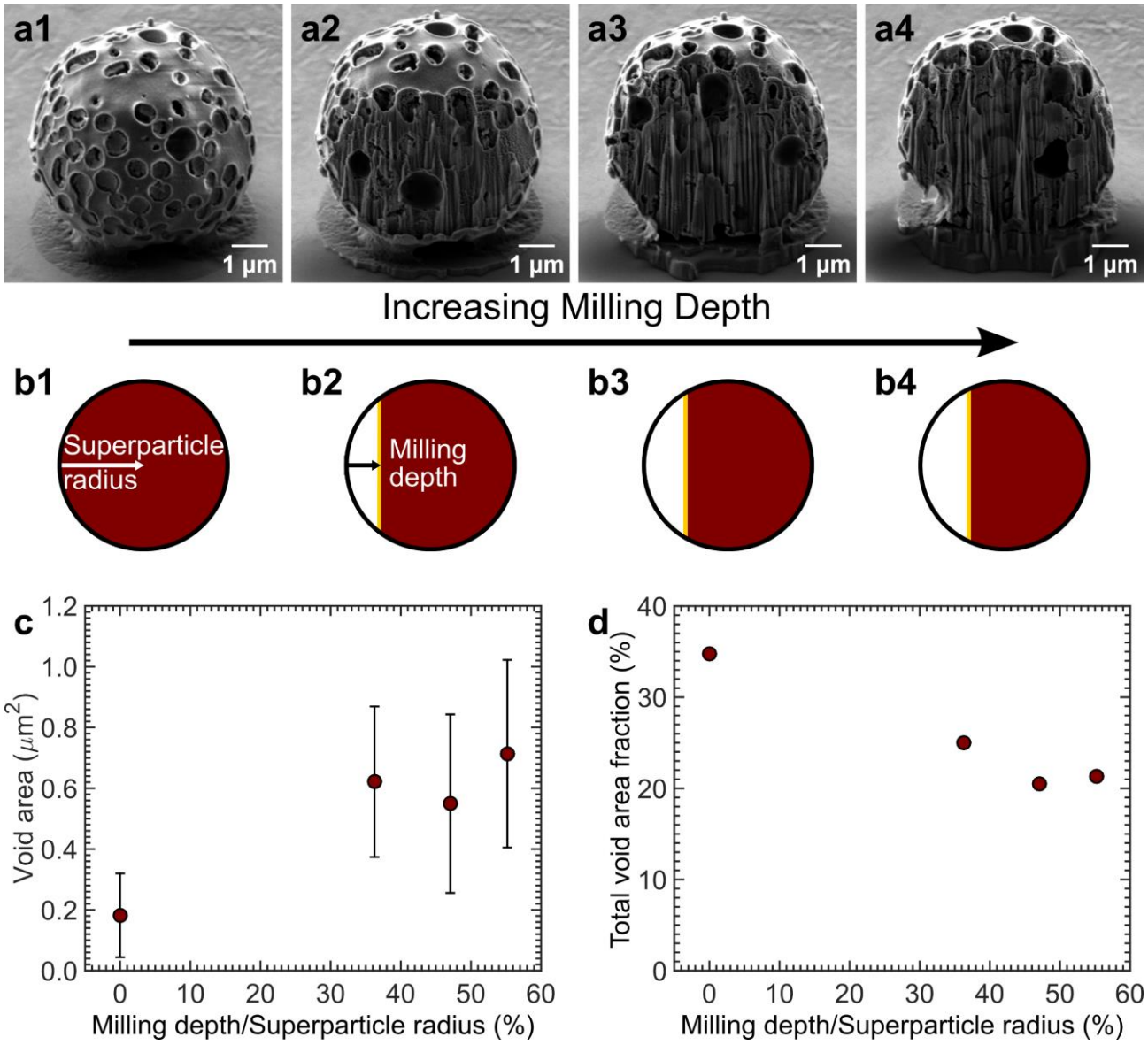

Figure 3: Investigation of the inner volume of the superparticles at the intermediate composition ($\phi = 0.5$). (a1-a4) Focused ion beam milling series of a single nanocrystal superparticle, and relative schematic (b1-b4). Statistical analysis of the area of the voids (c) and total void area fraction (d) as a function of distance from the surface of the superparticle. Markers indicate the mean value, while error bars indicate the standard deviation.

compositions ranging from $\phi = 0$, indicating superparticles containing solely Fe_3O_4 NCs, to $\phi = 1$, indicating superparticles containing solely CdSe/CdS NCs. The results are shown in the top panel of **Figure 2**. Superparticles comprising a single NC species, $\phi = 0$ or 1, resemble homogeneous spheres with smooth surfaces and minimal surface features. Interestingly, upon the incorporation of a second NC species at fractions $0.2 \leq \phi \leq 0.8$, the surface of the superparticles begins to deviate from smooth to show depressions, voids, and asperities. These features become most apparent at $\phi = 0.5$, as shown in the bottom panel of **Figure 2**, and are robust across several preparations, see **Figure S3**. A closer inspection of the scanning electron micrographs reveals cracks in the superparticle structure that are visible through the surface depressions, suggesting the presence of voids below the surface.

We investigate this hypothesis by milling a single NC superparticle with $\phi = 0.5$ using a focused-ion beam. Scanning electron micrographs taken after milling at different depths reveal the presence of spherical voids distributed throughout the volume of the spherical superparticle (**Figures 3a$_1$-a$_4$** and **3b$_1$-b$_4$** for images and schematics, respectively). Analyzing these images allows us to quantify the size of the voids as well as their spatial distribution within the superparticle. **Figure 3c** shows the area of the voids as projected on the milling plane as a function of milling depth. The area of the voids increases with milling depth by almost 4-fold, from 0.18 μm^2 at the surface of the superparticle to 0.71 μm^2 at 55% of the superparticle radius, corresponding to a 2-fold increase in void radius from 0.24 μm to 0.48 μm. While the size of the individual voids increases with milling depth, the total void area fraction decreases from 35% to 21% when moving from the surface to the center of the

superparticle. Overall, these measurements indicate the formation of larger yet fewer voids with increased distance from the superparticle surface.

We conduct Monte Carlo (MC) simulations to gain a deeper understanding of the driving forces governing the formation of voids inside the superparticles. We extend our previously developed lattice MC simulation protocol[67] on a discretized 3D lattice for expediency to model the NC assembly. Each system is initialized as a random dispersion of NC sites confined inside a spherical region that represents the densifying droplet. All remaining lattice sites within the spherical region not occupied by an NC are classified as a solvent site. Lattice sites that define the boundary of the spherical region are classified as a "wall" type. Our MC simulation implements four different move types for NCs – translation, rotation, cluster move, and emulsion densification (evaporation). Specifically, we define a translation move as a displacement of a NC by one lattice site. Similarly, a rotation move performs a rotational displacement of an NC by 90° relative to either the x-, y-, or z-axis of the lattice. Cluster move refers to perturbation of a group of neighboring NCs. We employ two types of perturbations: 1) reorganization of NCs within a cluster and 2) translation of a NC cluster as a whole. Evaporation moves are performed such that the solvent particle closest to the receding spherical wall is converted from a "solvent" type to a "wall" type. The converted site cannot be occupied by another NC or solvent particle. All MC moves are accepted/rejected using the standard Metropolis algorithm.[78] For rapid detection of clusters formation/break-up, we employ the *freud* analysis package.[79] To equilibrate the system, we first perform only translation and rotation moves for NC and solvent particles under athermal conditions for 1E6 MC steps. Afterwards, we turn on all relevant interactions between NCs and solvent particles and perform all MC move types for 1E7 MC steps. The initial volume fraction is 0.05, close to experiments. To control the rate at which we densify the system from the initial volume fraction in simulation, we define an evaporation rate (α) as the ratio of evaporation moves relative to other moves in the system. A value of α=0 indicates no evaporative move and α=1 indicates that all MC moves are evaporative moves.

To compute the relevant interaction energies, we assume that each lattice site containing a NC represents a unit cell of the self-assembled superlattice structure. Therefore, the physical picture that our simulation seeks to describe is that of interacting unit cells of NC superlattices that grow and merge with each other during emulsion densification, ultimately driving the formation of large crystalline domains of NC superparticles. This assumption builds on the numerous studies highlighting the propensity of NCs to self-assemble into crystalline morphologies under emulsion templating.[44-46, 51, 80-88] The interaction energies between NCs are then extracted as the per-unit cell lattice energy of formation computed using our previously developed thermodynamic perturbation theory (TPT), see Methods/SI for details [27, 89]

The results of our simulations for unary ($\phi = 0$ or *1)* and binary ($\phi = 0.5$) dispersions of NCs as a function of emulsion densification are shown in **Figure 4a-b** respectively. NCs with different compositions exhibit a strong tendency to phase-separate during assembly (**Figure 4b**). Surprisingly, our experimental results support this interpretation, as the elemental map of the cross section of a superparticle prepared for ϕ = 0.5 suggests the presence of Cadmium- and Iron-rich regions, see Figure S4. A visual inspection of the simulated cross section of the fully formed superparticles reveals the emergence of voids with increasing ϕ values (**Figure 4c**). This observation is also in qualitative agreement with experimental observations (**Figures 1-3**). For quantitative comparisons with experiments, we measure the void area as a function of distance from the superparticle surface. An approximate 3-fold increase of the void area going from the surface to the center of the superparticle is observed in simulation (**Figure 4d**). Additionally, the void area fraction shows a 1.8-fold decrease in total void area when moving from the surface to the center of the superparticle (**Figure 4d**). Both measurements are in excellent agreement with the experimental observations shown in **Figure 3**.

The ability of our simulation protocol to reproduce experimental results points to a good understanding of the relevant NC interactions driving void formation. Here, we leverage the insights provided by simulation to develop an analytical theory that incorporates experimental parameters such as the NC stoichiometric ratio ϕ, NC size ratio γ, and emulsion densification rate α to predict the final void fraction within the self-assembled NC superlattices. We posit that there are four major interactions contributing to the observed void formation: 1) lattice formation energy from NC crystallization, 2) repulsion between different NC types, 3) confinement energy from the evaporating emulsion, and 4) surface tension cost of NC contacts with the emulsion boundary and solvent. Our theory seeks to capture the following physical process. Growing crystallites of NCs are pushed together by the decrease in available volume due to emulsion densification. As densification progresses, clusters of NCs with the same composition can reorganize and merge, whereas those with different composition disfavor merging. In the dilute limit, clusters can move past each other without interacting. However, at higher densities NC clusters are larger and less mobile due to the limited space between neighboring particles, hindering rearrangements. The repulsion between incompatible NC types further undermines reorganization and drives void formation through phase separation.

An alternative way to think about this process is through the competition between kinetics and thermodynamics. If given enough time, the system will be thermodynamically driven to phase separate into pure phases for each NC species. The key force preventing this, however, lies in solvent removal which induces a shrinkage of the emulsion droplets. This densification provides an increasingly higher thermodynamic driving force for NC self-assembly into superlattices. This means that the size of the initial NC superlattice cluster grows with increasing densification. In the dilute regime, clusters consisting of NCs with different composition can move past each other to merge with more favorable clusters containing the same constitutive NC species. This will result in larger NC clusters when the emulsion reaches the high density regime. In this regime, these larger clusters exhibit slower diffusion within the emulsion droplets due to both their increased size and a higher local NC cluster

density. In other words, cluster reorganization and merging are hindered in the high density regime due to both decreased cluster mobility and increased repulsion with neighboring clusters due to phase separation driving forces. Eventually, the NC clusters become trapped in place, as the relaxation time needed to escape their confinement is longer than the densification time of the system. Therefore, the driving force that disfavors merging is a result of kinetics preventing NC mobility within an emulsion droplet of increasing concentration.

Using scaling theory, we balance this interplay between attractive and repulsive interactions between NCs along with the surface tension cost of NCs in contact with the solvent and the driving force from the densifying emulsion to predict the void fraction in the assembled system (**SI**). We obtain the following quadratic equation for the void volume fraction ϕ_V:

$$0 \sim \phi_V^2[D_1 - (5/9)D_2] + \phi_V[-2D_1 + (5/3)D_2] + [D_1 - D_2 + \Delta G_{solvent}] \quad (1)$$

where $D_1 = \chi_1 - \Delta G_{solvent}$ and $D_2 = {}^{2}/_{3}\, n_P^{-1/3}\chi_2(\alpha C + \Gamma)$ and χ_1 and χ_2 are defined as:

$$\chi_1 = \Delta G_{crys}[\phi^2 + (1-\phi)^2] - \Delta G_{rep}\phi(1-\phi) + \Delta G_{NC} \quad (2)$$

$$\chi_2 = \sigma_B^2[(1 - \phi + \phi^2)(x\gamma^3 + y)]^{2/3} \quad (3)$$

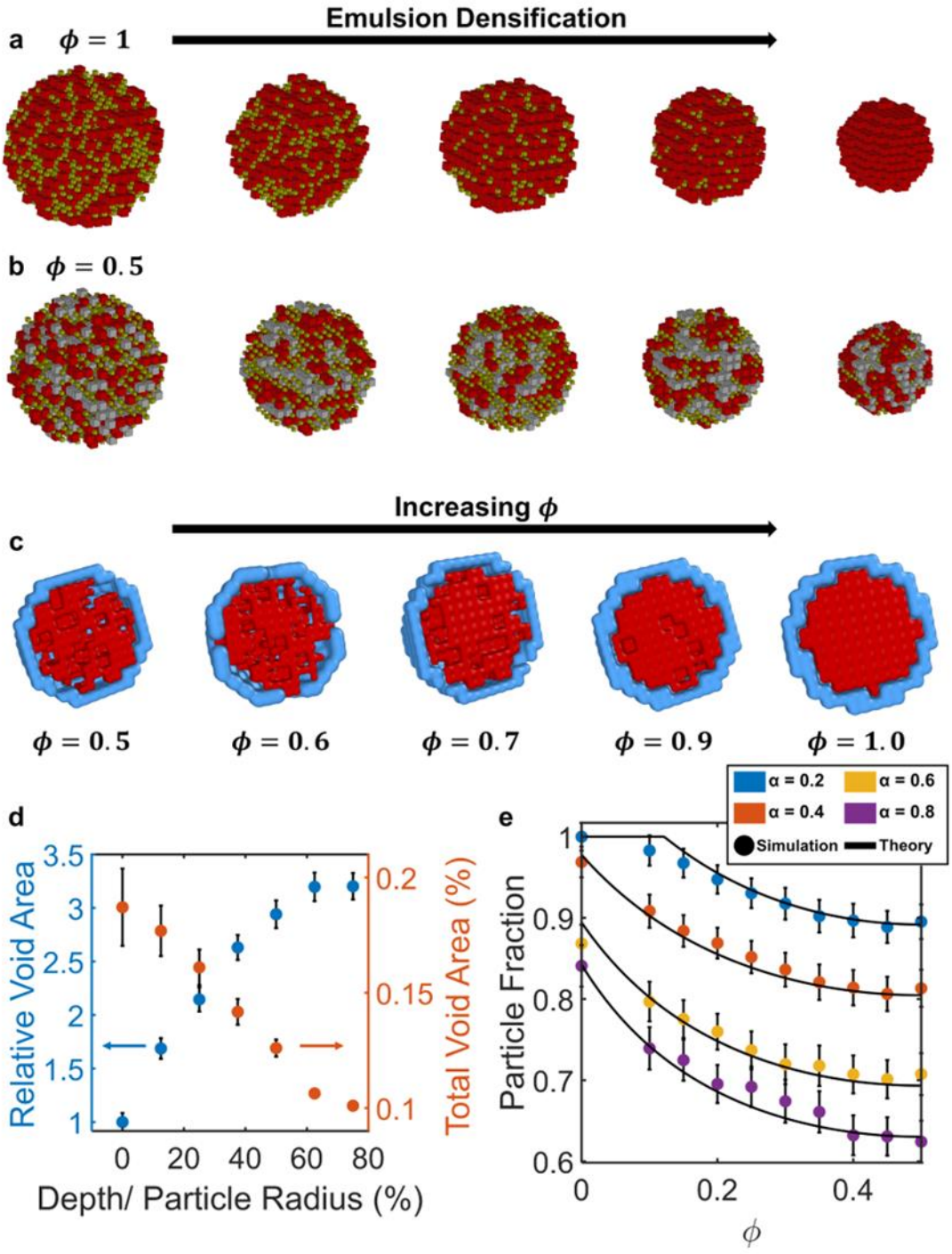

Figure 4: Computer simulations of porous superparticle self-assembly. Snapshots of nanocrystal (NC) superlattice assembly with increasing emulsion densification for (a) $\phi = 1.0$ and (b) $\phi = 0.5$. Red and gray particles represent the NCs, yellow particles represent the solvent. (c) Visualization of a cross-section of the self-assembled NC superlattice at different values of ϕ. The border of the superlattice is highlighted in blue. (d) Quantitative measurements of the relative void area and percentage of total void volume within a NC superparticle as a function of milling depth relative to the total superparticle radius. (e) Theoretical predictions of the final void fraction (**Equation 1**) as a function of ϕ and α. Solid lines indicate theory and data points are from simulations.

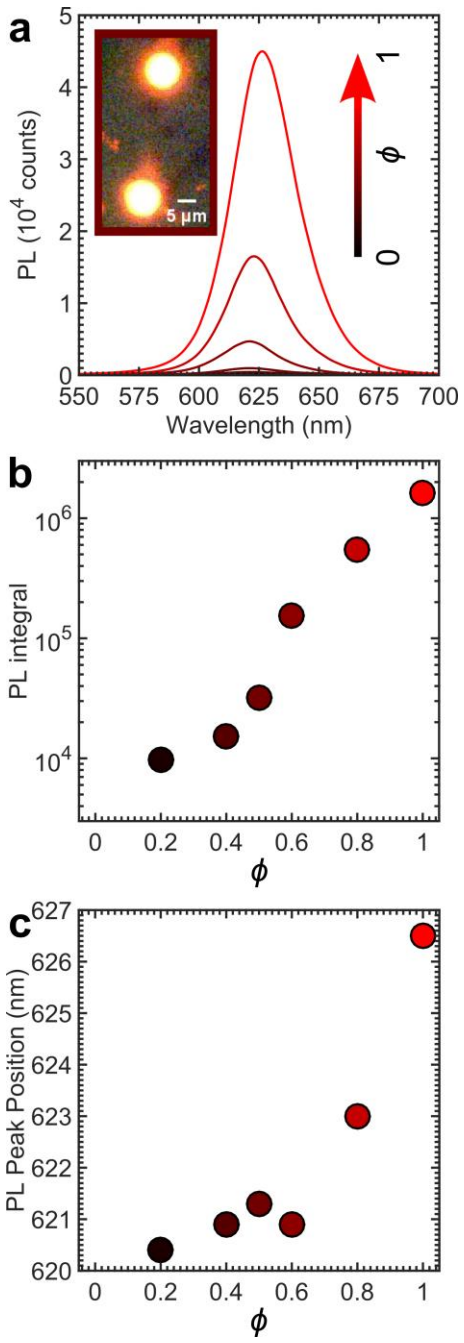

Figure 5: Photoluminescence (PL) of magneto-fluorescent, composite nanocrystal (NC) superparticles. (a) PL spectra of individual superparticles prepared with different compositions of NCs. Fe_3O_4 superparticles are non-emissive, therefore their spectra are not shown. The inset shows PL micrographs of two superparticles with ϕ = 0.5. (b) Integrated PL intensity and (c) spectral position of the PL peak of individual superparticles as a function of superparticle composition. Excitation wavelength: 420 nm.

Each free energy (ΔG) term is computed using TPT (**Methods/SI**), where ΔG_{crys} is the free energy of unit cell formation for a given lattice, ΔG_{NC} is the energy computed from Boltzmann-weighted averaging of amorphous NC clusters, ΔG_{rep} is the energy difference between a unit cell with heterogeneous versus homogeneous NC compositions, and $\Delta G_{solvent}$ is the Boltzmann weighted average energy of solvent clusters. The quantities x and y define the stoichiometry of the NC superattice (i.e. A_xB_y) and Γ indicates the surface tension cost of the crystal/solvent interface. **Equation 1** can be easily solved using the quadratic formula and provides excellent agreement when compared to results calculated from simulation (**Figure 4e**). These results predict that higher emulsion densification rates should lead to more porous superparticles. This might explain why previous synthetic procedures based on densification rates lower than those afforded by the source-sink emulsion approach did not produce porous superparticles even when using a very similar combination of NC species.[90] This renewed understanding paves the way to the control *a priori* of the porous structure of superparticles.

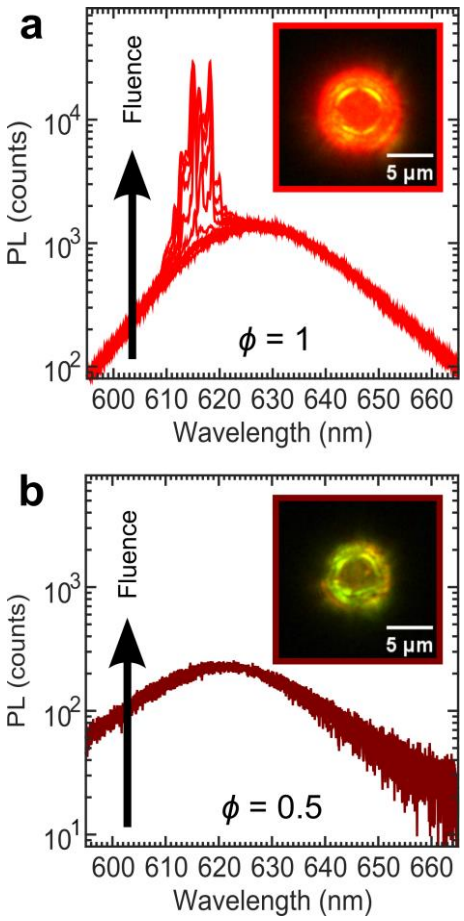

Figure 6: Lasing of magneto-fluorescent, composite nanocrystal superparticles. Photoluminescence (PL) spectra with increasing excitation fluence for ϕ = 1 (a) and ϕ = 0.5 (b). The inset shows photoluminescence micrographs of the superparticles. Excitation wavelength: 488 nm.

In addition to driving the assembly of porous superlattices, mixing Fe_3O_4 and CdSe/CdS NCs imbues the resulting superparticles with interesting optical effects. **Figure 5a** shows the photoluminescence (PL) spectra of individual magneto-fluorescent superparticles of different compositions, $0 \leq \phi \leq 1$, when excited with 420 nm light. The PL peak centered around 625 nm arises due to the emission from CdSe/CdS NCs, while the Fe_3O_4 are non-emissive. As the fraction of CdSe/CdS NCs in a superparticles increases from $\phi = 0.2$ to 1, the integrated PL intensity increases by more than two orders of magnitude (**Figure 5b**). Additionally, the position of the PL peak undergoes a 6.1 nm red-shift with increasing ϕ from 620.4 nm to 626.5 nm (**Figure 5c**). Both the total PL intensity and PL position change non-linearly with ϕ, with significant increase for $\phi > 0.5$.

Spherical NC superparticles can act as a resonant cavity, trapping light near their surface through photonic whispering-gallery modes.[48-50] When the excitation fluence overcomes the cavity's optical losses, the photons trapped in the whispering-gallery modes can induce lasing action. We investigate the role of an intermediate composition on the lasing properties of the composite superparticles. At $\phi = 1$, increasing the fluence of a 488 nm pulsed laser source on a single superparticle results in multi-mode lasing assisted by the tightly-spaced whispering-gallery modes, as shown in **Figure 6a**.[52] However, at $\phi = 0.5$, we are unable to trigger the lasing action **(Figure 6b).** Additionally, the intensity of the PL spectrum does not increase with excitation fluence, indicating optical saturation. This suggests the presence of additional optical losses in the cavity.

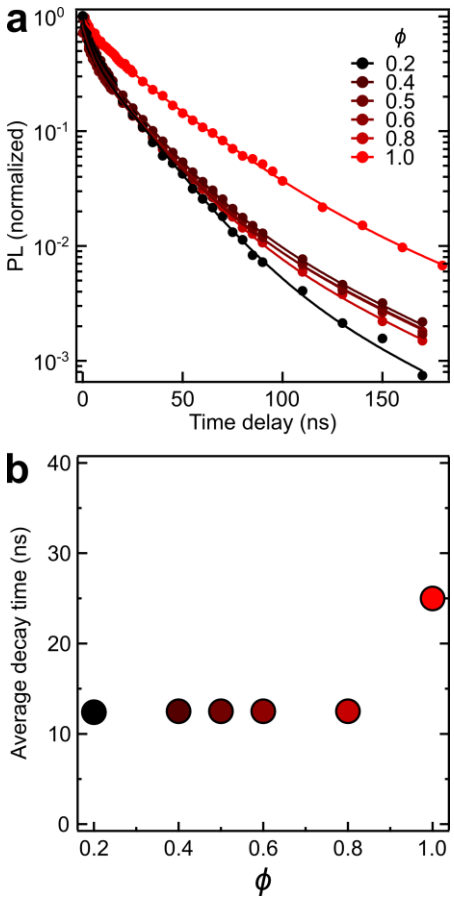

Figure 7: Photoluminescence (PL) kinetics of magneto-fluorescent, composite nanocrystal superparticles excited by pulsed laser light (5 ns duration, wavelength = 488 nm). (a) Kinetics of the emission intensity recorded at 625 nm, as observed for different compositions of the superparticles. Circles represent data points; full lines represent multi-exponential fits. (b) Average lifetime obtained by least-square fitting data in panel (a) with multi-exponential decay functions.

Comparable PL quenching was observed in the literature from a binary mixture of iron oxide and CdSe/ZnS NCs dispersed in octane droplets.[91] Studies on iron oxide NCs functionalized with fluorescent molecules,[92] or binary mixtures of iron oxide and CdSe/ZnS NCs co-encapsulated in micelles[93] suggest that PL quenching increases when the distance between NCs decreases. However, the distance between NCs of two different species in a well-mixed system should depend linearly on the relative volume fraction of the two species. This should result in a linear change of the total PL intensity with superparticle composition (ϕ). Instead, the integrated PL signal changes non-linearly with superparticle composition, **Figure 5b.** This suggests the onset of phase separation of the two NC species at intermediate compositions.

We investigate this hypothesis by nanosecond-time-resolved fluorescence measurements. **Figure 7a** shows the emission decay kinetics observed for different compositions ϕ of the superparticles. The excited-state depopulation of pure CdSe/CdS superparticles ($\phi=1$) follows multi-exponential kinetics. The data are fitted by a linear combination of three time constants (τ_i) of different amplitudes (A_i): 8.0 ns (31%), 30 ns (65%), 80 ns (4%).[75] However, upon addition of Fe_3O_4 NCs ($\phi=0.8$) the decay kinetics become shorter across all 3 components (see **Table S1**). The average lifetime, defined as $\tau_{av} = \sum_{i=1-3} A_i\tau_i / \sum_{i=1-3} A_i$ (**Figure 7b**), decreases to half of its initial value, from 25.2 ns ($\phi=1$) to 12.5 ns ($\phi=0.8$). Interestingly, increasing the concentration of Fe_3O_4 NCs even further does not lead to a change in the average lifetime, indicating saturation already at $\phi=0.8$.

These results show that Fe_3O_4 NCs are capable of quenching excited-state carriers in CdSe/CdS NCs by introducing additional non-radiative decay pathways which shorten the excited-state lifetime. The Fe_3O_4 NCs display a quasi-continuum of absorption transitions overlapping with the emission from CdSe/CdS NCs (**Figure S1**). Thus, we identify a possible quenching mechanism in non-radiative energy transfer from the emissive transitions of CdSe/CdS NCs to nearby Fe_3O_4 NCs. Förster-theory calculations yield a Förster radius (the distance at which a 2-fold reduction in PL quantum yield is expected) of 6.5 nm.[94-96] This value is consistent with the interval ranging from the minimum surface-to-surface distance (~2 nm)[46, 80] and the center-to-center distance (13 nm) between two neighboring NCs. Since at $\phi=0.8$ most CdSe/CdS NCs will find at least one Fe_3O_4 NC among their six nearest neighbors, the initial lifetime reduction can be explained by non-radiative energy transfer, These close-range interactions also explain the shift of the PL peak (**Figure 5c**), which almost entirely happens between $\phi=0.8$ and *1*, as the emission peak position is expected to be highly sensitive to the local dielectric environment of the emitting NCs.[52]

The lack of further changes in the decay kinetics for $\phi<0.8$ indicates that the additional Fe_3O_4 NCs are too far from the CdSe/CdS emitters to have any additional effects on their radiative or non-radiative rate. Even the configurations where a given CdSe/CdS NC interacts with more than one nearest-neighbor Fe_3O_4 NCs must be rare, otherwise we should observe a multiplicity of decay patterns associated to these different configurations. In contrast, the kinetics in **Figure 7a** are identical for any $\phi<1$. We conclude that time-resolved PL data further support the phase separation of the two NC species at intermediate compositions, in strong agreement with the results of simulations (**Figure 4b**). After the onset of phase separation ($\phi<0.8$), the further reduction of the emission quantum yield of the superparticles (**Figure 5b**) does not stem from direct electronic interactions between the two types of NCs. Rather, it can be explained by the increased reabsorption from Fe_3O_4 NCs of photons emitted by CdSe/CdS NCs, and by the growing contribution of non-emissive Fe_3O_4 NCs to the absorption of excitation light.

CONCLUSION:

We showed a direct assembly pathway that gives rise to the formation of porous, magneto-fluorescent superparticles by leveraging the repulsive colloidal interactions between NCs with different compositions: super-paramagnetic Fe_3O_4 and semiconductor CdSe/CdS NCs. The confinement of colloidal NCs to toluene droplets undergoing rapid densification through the source-sink emulsion process leads to monodisperse, spherical superparticles. Whereas superparticles consisting of a single NC species (ϕ=0 or 1) show smooth surfaces, superparticles with intermediate compositions ($0.2 \leq \phi \leq 0.8$) show the presence of circular depressions. These features are not limited to the surface of the superparticles but instead extend to their inner volume as spherical voids. Molecular simulations further reveal that the repulsion between NCs with different compositions favors phase separation inside the densifying emulsion, driving the formation of the voids observed in the final superstructures. The characteristics, occurrence, and spatial distribution of these voids in simulations matches well with experimental results, confirming that using a composition characterized by equal volumes of the two NC species maximizes the porosity of the superparticle.

Analyzing the significant composition-dependent changes in the optical and photonic properties of the superparticles, namely the occurrence or inhibition of the lasing action and PL saturation, provides an independent confirmation of the phase separation between emissive CdSe/CdS and non-emissive Fe_3O_4 NCs at intermediate compositions. Based on this excellent agreement between experiments and simulations, we developed a theory that predicts the porosity of the final superparticles from the experimentally controlled parameters controlled in experiment such as the NC stoichiometry, NC size ratio γ, and the rate of densification of the emulsion droplets α. These results provide a clear roadmap to design confined, high surface area, porous, multifunctional superparticles. These superparticles may be used in catalytic or on demand delivery applications: Excitation with high-frequency magnetic fields may heat and release the stored cargo,[97] and the release may be monitored optically by changes in refractive index of the superparticle.[52, 98-103] Finally, future structural designs of the assembled structures may allow for interesting developments in the manipulation of the magnetic properties of the final material.[6]

METHODS

NC synthesis: Fe_3O_4 and CdSe/CdS NCs are synthesized according to the literature[74, 75] with minor changes that are outlined in detail in our latest works.[48, 80] After washing, the NCs are dispersed in toluene at a volume fraction of 0.01% and filtered using 0.22 μm PVDF syringe filters.

Transmission electron microscopy: The NCs are deposited (10 μL at ~0.1 mg/mL) on a carbon-coated TEM grid and placed under vacuum for 1 hour prior to imaging. The grid is imaged by using a JEOL F200 microscope operated at 200 kV. During imaging, magnification, focus, and tilt angle are varied.

Superparticle synthesis: Monodisperse NC superparticles were prepared by using the source-sink emulsion system aided by droplet microfluidics. The procedure is described in detail in our latest works.[48, 50, 52] Briefly, we use a multichannel pressure regulator (Elveflow, OB1MK3+) connected to a glass microfluidic chip (Darwin Microfluidics, model T-26) with two cross junctions to mix three distinct phases: the dispersed phase (NCs in toluene at 0.01% volume fraction, ϕ = [0,1]), the continuous phase (20 mM sodium dodecyl sulfate in water), and the "sink" emulsion phase (55 nm droplets of hexadecane-in-water, 1% w/w, prepared just before through extended tip sonication), see **Figure 1**. The first junction of the microfluidic chip is used to generate monodisperse toluene-in-water droplets containing the NCs, generating the "source" emulsion. The second junction is used to mix this source emulsion with the sink emulsion. The length of the PFA tubing determines the co-residence time of the two emulsions of ~ 4 min. During this time, the emulsions are kept at a temperature of 50 °C to facilitate the migration of toluene from the source to the sink emulsion. The sample is collected in 20 mL scintillation vials that initially contain 5 mL of sink emulsion. The vials are left uncapped overnight on a hot plate set at 50 °C. The samples are then washed 3-fold in the dispersed phase by using mild (100 g) centrifugation in glass containers. Finally, the superparticles were redispersed in 10 mM sodium dodecyl sulfate in water.

Scanning electron microscopy: The samples are prepared for imaging by drop casting 40 μL of the superparticle dispersion on a clean piece of silicon wafer, followed by drying. The wafer is then dipped twice in a cleaning solution of water to isopropanol 1:2 (v/v) to remove excess surfactant, followed by vacuum drying. The samples are imaged by using a Tescan S8252X operated at 2 kV and 100 pA. FIB milling is performed with an ion voltage of 30 kV and a current of 100 nA. Image analysis is performed by using ImageJ.

Steady-state PL measurements on single superparticles: PL spectra are collected using a CRAIC 308 PV microspectrophotometer integrated on an Olympus BX51 equipped with a 120 W mercury vapor arc lamp as the excitation source. The excitation light is filtered by a 400 nm – 440 nm band-pass filter, and the emission is collected through a 475 nm long-pass filter (Olympus U-MWBV2). The integration time is set to 1 s, and the number of averaged spectra is set to 30.

Time-resolved PL measurements: Superparticles are drop-casted on a glass slide (10 μL of dispersion and 40 μL of water) and allowed to dry under vacuum. The glass slide is then dipped 3 times in a solution of 33% water and 67% isopropanol and allowed to dry under vacuum. Drop-cast superparticles are excited by 5 ns laser pulses provided by an optical parametric oscillator pulsed by the third harmonic of a Nd:YAG Q-switched laser. The emission from the samples is collected by a lens and directed to the entrance slit of a monochromator coupled to an intensified CCD camera triggered by the laser. Emission spectra from the samples, time-gated in temporal windows variably delayed from the excitation pulse, are recorded to reconstruct the emission intensity kinetics.

Lasing experiments on single superparticles: Lasing spectra are collected on a home-built confocal microscope: an ultrafast laser (Coherent Monaco 1035, 272 fs pulse width, 1kHz repetition rate) pumps an optical parametric amplifier (Coherent OperaHP), which is set to output 488 nm light. The beam passes a 500 nm short-pass filter and a computer-controlled gradient neutral density filter to adjust the incident fluence. The light is coupled to a meter-long, 105 μm core, 0.1 NA optical fiber. Light exiting the fiber is collimated by a 30 mm focal length lens and is sent to the infinity space of a modified Olympus BX43 microscope. The light is then imaged to the sample surface by a 50x, 0.8 NA objective lens (Olympus MPLFLN50XBD), which yields a spot size of approximately 12 μm completely covering a single superparticle. The emitted light is collected through the same objective, passes the microscope tube lens, and is then filtered (500 nm long-pass) to remove the excitation beam. Light is then split by a 30:70 beam splitter; one path is coupled to a collection optical fiber (105 μm core, 0.1 NA), which is relayed to a spectrometer (Horiba iHR 550 monochromator and Symphony II liquid nitrogen cooled CCD), while the other path is sent to a CCD camera (Thorlabs DCU224C) for the acquisition of PL images.

Förster radius calculation: The Förster radius is estimated by calculating the overlap integral between the normalized photoluminescence band of the donor CdSe/CdSe NC and the absorption spectrum of the acceptor Fe_3O_4 NC and using the classical expression found in the literature.[96]

Lattice Monte Carlo simulation of NC self-assembly: We conducted simulations spanning sweep across a phase design space defined by different densification rates ($\alpha \in [0,1]$) and fraction of CdSe/CdS relative to the total number of NCs ($\phi \in [0,0.5]$). Each simulation is initialized in the dilute limit with NC volume fraction ≤1% confined within a spherical region. MC move types are: translation, rotation, cluster, and densification (solvent evaporation). Cluster moves employ both translation and rotation moves, weighted equally. All moves are rejected/accepted using the standard Metropolis algorithm. All simulations are are run for 1E7 MC moves to ensure equilibration.

Thermodynamic perturbation theory for free energy of lattice formation: We define a "hard-particle" reference for NCs occupying different lattice structures of interest. We then assign an interaction potential $V(r)$ between NCs to compute the excess free energy of formation. For our purposes, we use a Mie-type potential that has been successfully employed to model binary spherical NCs assembly in simulations. The equilibrium constant K for the formation of the lattice is computed using: $K = \prod_i \sum_j \frac{\rho^{s_{ij}}}{s_{ij!}} \int f_{ij}^{s_{ij}}(r) g_{ij,c}(r) d\vec{r}$, where the product and summation over i and j are performed over all types of interactions and NC types, respectively. The function $f(r)$ is the Mayer-f function defined as $f(r) = e^{-\beta V(r)} - 1$, ρ is the system density, and $g_c(r)$ and s are the radial distribution function and coordination number of the crystal of interest, respectively. Using thermodynamics, the excess free energy $\Delta G = -kT \ln K$. For full details of the derivation, we refer the read to our previously published works.[27, 89]

ASSOCIATED CONTENT

Supporting Information. Optical absorption spectra of nanocrystals (Figure S1), optical micrographs of source droplets (Figure S2), electron micrographs of multiple superparticles samples (Figure S3), elemental map of the cross section of a superparticle (Figure S4), additional information on the simulation framework (theoretical development, scaling model for lattice size, nanocrystal lattice formation and total interaction energy, lattice Monte Carlo simulation) can be found in the supporting information file. This material is available free of charge via the Internet at http://pubs.acs.org.

AUTHOR INFORMATION

Corresponding Author

*Email: cbmurray@sas.upenn.edu, sglotzer@umich.edu, emanuele.marino@unipa.it

Author Contributions

†These authors contributed equally to the manuscript.
E.M. synthesized and imaged the superparticles, T.V. derived the theory and performed the simulations and subsequent analysis, D.J.R. performed the TEM studies, S.J.N. performed the lasing measurements, H.B. and E.M. performed the steady-state optical measurements,

A.S., F.M., M.C., and E.M. performed the time-resolved optical measurements, A.W.K. synthesized the Fe_3O_4 nanocrystals, C.B.M. and S.C.G. supervised the project. The manuscript was written through contributions of all authors. All authors have given approval to the final version of the manuscript.

ACKNOWLEDGMENT

E.M. and C.B.M acknowledge support from the National Science Foundation under Grant No. DMR-2019444 for the superparticle synthesis and characterization. E.M. acknowledges travel support from the National Science Foundation under the IMOD Integrative Travel Program Award, Grant No. DMR-2019444, and from the European Commission - Horizon Europe - Next Generation Internet Enrichers programme, Grant Agreement No. 101070125. E.M. is grateful to the European Union – NextGenerationEU – funding MUR D.M. 737/2021 for funding his position at Unipa. E.M. acknowledges the Fondo Finalizzato Alla Ricerca Di Ateneo (FFR) 2022-2024 of Unipa for funding. E.M. and M.C. acknowledge the European Union NextGenerationEU, Project code PE0000021, CUP UNIPA B73C22001280006, Project title "Network 4 Energy Sustainable Transition – NEST for funding. T.V. and S.C.G. acknowledge support from the Office of Naval Research Multidisciplinary University Research Initiative (MURI) Award ONR N00014-18-1-2497 for the theory and simulation development. A.W.K. and C.R.K. acknowledge support from the Semiconductor Research Corporation (SRC) under the Nanomanufacturing Materials and Processes (NMP) trust via Task 2797.001 for part of the SEM imaging. S.J.N and C.R.K. acknowledge the National Science Foundation (NSF) through the University of Pennsylvania Materials Research Science and Engineering Center (MRSEC) under Award No. DMR-1720530 for the lasing experiments.

REFERENCES

1. Nagaoka, Y.; Suda, M.; Yoon, I.; Chen, N.; Yang, H.; Liu, Y.; Anzures, B. A.; Parman, S. W.; Wang, Z.; Grünwald, M.; Yamamoto, H. M.; Chen, O., Bulk Grain-Boundary Materials from Nanocrystals. *Chem* **2021,** *7* (2), 509-525.
2. Urban, J. J.; Talapin, D. V.; Shevchenko, E. V.; Murray, C. B., Self-Assembly of PbTe Quantum Dots into Nanocrystal Superlattices and Glassy Films. *Journal of the American Chemical Society* **2006,** *128* (10), 3248-3255.
3. Murray, C. B.; Kagan, C. R.; Bawendi, M. G., Self-Organization of CdSe Nanocrystallites into Three-Dimensional Quantum Dot Superlattices. *Science* **1995,** *270* (5240), 1335-1338.
4. Shevchenko, E. V.; Talapin, D. V.; Kotov, N. A.; O'Brien, S.; Murray, C. B., Structural diversity in binary nanoparticle superlattices. *Nature* **2006,** *439* (7072), 55-59.
5. Nykypanchuk, D.; Maye, M. M.; van der Lelie, D.; Gang, O., DNA-guided crystallization of colloidal nanoparticles. *Nature* **2008,** *451* (7178), 549-552.
6. Marino, E.; LaCour, R. A.; Moore, T. C.; van Dongen, S. W.; Keller, A. W.; An, D.; Yang, S.; Rosen, D. J.; Gouget, G.; Tsai, E. H. R.; Kagan, C. R.; Kodger, T. E.; Glotzer, S. C.; Murray, C. B., Crystallization of binary nanocrystal superlattices and the relevance of short-range attraction. *Nature Synthesis* **2024** volume 3, pages 111–122.
7. Talapin, D. V.; Shevchenko, E. V.; Bodnarchuk, M. I.; Ye, X.; Chen, J.; Murray, C. B., Quasicrystalline order in self-assembled binary nanoparticle superlattices. *Nature* **2009,** *461* (7266), 964-967.
8. Ye, X.; Chen, J.; Eric Irrgang, M.; Engel, M.; Dong, A.; Glotzer, Sharon C.; Murray, C. B., Quasicrystalline nanocrystal superlattice with partial matching rules. *Nature Materials* **2017,** *16* (2), 214-219.
9. Nagaoka, Y.; Zhu, H.; Eggert, D.; Chen, O., Single-component quasicrystalline nanocrystal superlattices through flexible polygon tiling rule. *Science* **2018,** *362* (6421), 1396-1400.
10. Paik, T.; Murray, C. B., Shape-Directed Binary Assembly of Anisotropic Nanoplates: A Nanocrystal Puzzle with Shape-Complementary Building Blocks. *Nano Letters* **2013,** *13* (6), 2952-2956.
11. Gordon, T. R.; Paik, T.; Klein, D. R.; Naik, G. V.; Caglayan, H.; Boltasseva, A.; Murray, C. B., Shape-Dependent Plasmonic Response and Directed Self-Assembly in a New Semiconductor Building Block, Indium-Doped Cadmium Oxide (ICO). *Nano Letters* **2013,** *13* (6), 2857-2863.
12. Ye, X.; Millan, J. A.; Engel, M.; Chen, J.; Diroll, B. T.; Glotzer, S. C.; Murray, C. B., Shape Alloys of Nanorods and Nanospheres from Self-Assembly. *Nano Letters* **2013,** *13* (10), 4980-4988.
13. Abbas, A. S.; Vargo, E.; Jamali, V.; Ercius, P.; Pieters, P. F.; Brinn, R. M.; Ben-Moshe, A.; Cho, M. G.; Xu, T.; Alivisatos, A. P., Observation of an Orientational Glass in a Superlattice of Elliptically-Faceted CdSe Nanocrystals. *ACS Nano* **2022,** *16* (6), 9339-9347.
14. Cherniukh, I.; Rainò, G.; Stöferle, T.; Burian, M.; Travesset, A.; Naumenko, D.; Amenitsch, H.; Erni, R.; Mahrt, R. F.; Bodnarchuk, M. I.; Kovalenko, M. V., Perovskite-type superlattices from lead halide perovskite nanocubes. *Nature* **2021,** *593* (7860), 535-542.
15. Cherniukh, I.; Rainò, G.; Sekh, T. V.; Zhu, C.; Shynkarenko, Y.; John, R. A.; Kobiyama, E.; Mahrt, R. F.; Stöferle, T.; Erni, R.; Kovalenko, M. V.; Bodnarchuk, M. I., Shape-Directed Co-Assembly of Lead Halide Perovskite Nanocubes with Dielectric Nanodisks into Binary Nanocrystal Superlattices. *ACS Nano* **2021,** *15* (10), 16488-16500.
16. Cherniukh, I.; Sekh, T. V.; Rainò, G.; Ashton, O. J.; Burian, M.; Travesset, A.; Athanasiou, M.; Manoli, A.; John, R. A.; Svyrydenko, M.; Morad, V.; Shynkarenko, Y.; Montanarella, F.; Naumenko, D.; Amenitsch, H.; Itskos, G.; Mahrt, R. F.; Stöferle, T.; Erni, R.; Kovalenko, M. V.; Bodnarchuk, M. I., Structural Diversity in Multicomponent Nanocrystal Superlattices Comprising Lead Halide Perovskite Nanocubes. *ACS Nano* **2022,** *16* (5), 7210-7232.
17. Jishkariani, D.; Elbert, K. C.; Wu, Y.; Lee, J. D.; Hermes, M.; Wang, D.; van Blaaderen, A.; Murray, C. B., Nanocrystal Core Size and Shape Substitutional Doping and Underlying Crystalline Order in Nanocrystal Superlattices. *ACS Nano* **2019,** *13* (5), 5712-5719.
18. Nagaoka, Y.; Tan, R.; Li, R.; Zhu, H.; Eggert, D.; Wu, Y. A.; Liu, Y.; Wang, Z.; Chen, O., Superstructures generated from truncated tetrahedral quantum dots. *Nature* **2018,** *561* (7723), 378-382.
19. Miszta, K.; de Graaf, J.; Bertoni, G.; Dorfs, D.; Brescia, R.; Marras, S.; Ceseracciu, L.; Cingolani, R.; van Roij, R.; Dijkstra, M.; Manna, L., Hierarchical self-assembly of suspended branched colloidal nanocrystals into superlattice structures. *Nature Materials* **2011,** *10* (11), 872-876.
20. LaCour, R. A.; Moore, T. C.; Glotzer, S. C., Tuning Stoichiometry to Promote Formation of Binary Colloidal Superlattices. *Physical Review Letters* **2022,** *128* (18), 188001.
21. Coropceanu, I.; Boles, M. A.; Talapin, D. V., Systematic Mapping of Binary Nanocrystal Superlattices: The Role of Topology in Phase Selection. *Journal of the American Chemical Society* **2019,** *141* (14), 5728-5740.

22. Elbert Katherine, C.; Zygmunt, W.; Vo, T.; Vara Corbin, M.; Rosen Daniel, J.; Krook Nadia, M.; Glotzer Sharon, C.; Murray Christopher, B., Anisotropic nanocrystal shape and ligand design for co-assembly. *Science Advances* **2021,** *7* (23), eabf9402.
23. Santos, P. J.; Gabrys, P. A.; Zornberg, L. Z.; Lee, M. S.; Macfarlane, R. J., Macroscopic materials assembled from nanoparticle superlattices. *Nature* **2021,** *591* (7851), 586-591.
24. Liu, Y.; Klement, M.; Wang, Y.; Zhong, Y.; Zhu, B.; Chen, J.; Engel, M.; Ye, X., Macromolecular Ligand Engineering for Programmable Nanoprism Assembly. *Journal of the American Chemical Society* **2021,** *143* (39), 16163-16172.
25. Winslow, S. W.; Smilgies, D.-M.; Swan, J. W.; Tisdale, W. A., Reversible Temperature-Induced Structural Transformations in PbS Nanocrystal Superlattices. *The Journal of Physical Chemistry C* **2020,** *124* (24), 13456-13466.
26. Winslow, S. W.; Swan, J. W.; Tisdale, W. A., The Importance of Unbound Ligand in Nanocrystal Superlattice Formation. *Journal of the American Chemical Society* **2020,** *142* (21), 9675-9685.
27. Lu, F.; Vo, T.; Zhang, Y.; Frenkel, A.; Yager Kevin, G.; Kumar, S.; Gang, O., Unusual packing of soft-shelled nanocubes. *Science Advances* **2019,** *5* (5), eaaw2399.
28. Marino, E.; Balazs, D. M.; Crisp, R. W.; Hermida-Merino, D.; Loi, M. A.; Kodger, T. E.; Schall, P., Controlling Superstructure–Property Relationships via Critical Casimir Assembly of Quantum Dots. *The Journal of Physical Chemistry C* **2019,** *123* (22), 13451-13457.
29. Vasilyev, O. A.; Marino, E.; Kluft, B. B.; Schall, P.; Kondrat, S., Debye vs. Casimir: controlling the structure of charged nanoparticles deposited on a substrate. *Nanoscale* **2021,** *13* (13), 6475-6488.
30. Zhang, H.; Dasbiswas, K.; Ludwig, N. B.; Han, G.; Lee, B.; Vaikuntanathan, S.; Talapin, D. V., Stable colloids in molten inorganic salts. *Nature* **2017,** *542* (7641), 328-331.
31. Coropceanu, I.; Janke Eric, M.; Portner, J.; Haubold, D.; Nguyen Trung, D.; Das, A.; Tanner Christian, P. N.; Utterback James, K.; Teitelbaum Samuel, W.; Hudson ¸ Margaret, H.; Sarma Nivedina, A.; Hinkle Alex, M.; Tassone Christopher, J.; Eychmüller, A.; Limmer David, T.; Olvera de la Cruz, M.; Ginsberg Naomi, S.; Talapin Dmitri, V., Self-assembly of nanocrystals into strongly electronically coupled all-inorganic supercrystals. *Science* **2022,** *375* (6587), 1422-1426.
32. Zhao, Q.; Gouget, G.; Guo, J.; Yang, S.; Zhao, T.; Straus, D. B.; Qian, C.; Oh, N.; Wang, H.; Murray, C. B.; Kagan, C. R., Enhanced Carrier Transport in Strongly Coupled, Epitaxially Fused CdSe Nanocrystal Solids. *Nano Letters* **2021,** *21* (7), 3318-3324.
33. Whitworth, G. L.; Dalmases, M.; Taghipour, N.; Konstantatos, G., Solution-processed PbS quantum dot infrared laser with room-temperature tunable emission in the optical telecommunications window. *Nature Photonics* **2021,** *15* (10), 738-742.
34. Han, D.; Jiao, Y.; Han, W.; Wu, G.; Li, T.; Yang, D.; Dong, A., A molecular-based approach for the direct synthesis of highly-ordered, homogeneously-doped mesoporous carbon frameworks. *Carbon* **2018,** *140*, 265-275.
35. You, B.; Jiang, N.; Sheng, M.; Bhushan, M. W.; Sun, Y., Hierarchically Porous Urchin-Like Ni2P Superstructures Supported on Nickel Foam as Efficient Bifunctional Electrocatalysts for Overall Water Splitting. *ACS Catalysis* **2016,** *6* (2), 714-721.
36. You, B.; Sun, Y., Hierarchically Porous Nickel Sulfide Multifunctional Superstructures. *Advanced Energy Materials* **2016,** *6* (7), 1502333.
37. Liu, X.; Kent, N.; Ceballos, A.; Streubel, R.; Jiang, Y.; Chai, Y.; Kim Paul, Y.; Forth, J.; Hellman, F.; Shi, S.; Wang, D.; Helms Brett, A.; Ashby Paul, D.; Fischer, P.; Russell Thomas, P., Reconfigurable ferromagnetic liquid droplets. *Science* **2019,** *365* (6450), 264-267.
38. Marino, E.; Vasilyev, O. A.; Kluft, B. B.; Stroink, M. J. B.; Kondrat, S.; Schall, P., Controlled deposition of nanoparticles with critical Casimir forces. *Nanoscale Horizons* **2021,** *6* (9), 751-758.
39. Lewis, D. J.; Zornberg, L. Z.; Carter, D. J. D.; Macfarlane, R. J., Single-crystal Winterbottom constructions of nanoparticle superlattices. *Nature Materials* **2020,** *19* (7), 719-724.
40. Wu, L.; Willis, J. J.; McKay, I. S.; Diroll, B. T.; Qin, J.; Cargnello, M.; Tassone, C. J., High-temperature crystallization of nanocrystals into three-dimensional superlattices. *Nature* **2017,** *548* (7666), 197-201.
41. Dong, A.; Chen, J.; Vora, P. M.; Kikkawa, J. M.; Murray, C. B., Binary nanocrystal superlattice membranes self-assembled at the liquid–air interface. *Nature* **2010,** *466* (7305), 474-477.
42. Dong, A.; Chen, J.; Oh, S. J.; Koh, W.-k.; Xiu, F.; Ye, X.; Ko, D.-K.; Wang, K. L.; Kagan, C. R.; Murray, C. B., Multiscale Periodic Assembly of Striped Nanocrystal Superlattice Films on a Liquid Surface. *Nano Letters* **2011,** *11* (2), 841-846.
43. Shim, H.-W.; Lim, A.-H.; Kim, J.-C.; Jang, E.; Seo, S.-D.; Lee, G.-H.; Kim, T. D.; Kim, D.-W., Scalable One-pot Bacteria-templating Synthesis Route toward Hierarchical, Porous-Co3O4 Superstructures for Supercapacitor Electrodes. *Scientific Reports* **2013,** *3* (1), 2325.
44. Lacava, J.; Born, P.; Kraus, T., Nanoparticle Clusters with Lennard-Jones Geometries. *Nano Letters* **2012,** *12* (6), 3279-3282.
45. de Nijs, B.; Dussi, S.; Smallenburg, F.; Meeldijk, J. D.; Groenendijk, D. J.; Filion, L.; Imhof, A.; van Blaaderen, A.; Dijkstra, M., Entropy-driven formation of large icosahedral colloidal clusters by spherical confinement. *Nature Materials* **2015,** *14* (1), 56-60.
46. Marino, E.; Kodger, T. E.; Wegdam, G. H.; Schall, P., Revealing Driving Forces in Quantum Dot Supercrystal Assembly. *Advanced Materials* **2018,** *30* (43), 1803433.
47. Wintzheimer, S.; Granath, T.; Oppmann, M.; Kister, T.; Thai, T.; Kraus, T.; Vogel, N.; Mandel, K., Supraparticles: Functionality from Uniform Structural Motifs. *ACS Nano* **2018,** *12* (6), 5093-5120.
48. Marino, E.; van Dongen, S. W.; Neuhaus, S. J.; Li, W.; Keller, A. W.; Kagan, C. R.; Kodger, T. E.; Murray, C. B., Monodisperse Nanocrystal Superparticles through a Source–Sink Emulsion System. *Chemistry of Materials* **2022,** *34* (6), 2779-2789.
49. Montanarella, F.; Urbonas, D.; Chadwick, L.; Moerman, P. G.; Baesjou, P. J.; Mahrt, R. F.; van Blaaderen, A.; Stöferle, T.; Vanmaekelbergh, D., Lasing Supraparticles Self-Assembled from Nanocrystals. *ACS Nano* **2018,** *12* (12), 12788-12794.
50. Neuhaus, S. J.; Marino, E.; Murray, C. B.; Kagan, C. R., Frequency Stabilization and Optically Tunable Lasing in Colloidal Quantum Dot Superparticles. *Nano Letters* **2023,** *23* (2), 645-651.
51. Marino, E.; Sciortino, A.; Berkhout, A.; MacArthur, K. E.; Heggen, M.; Gregorkiewicz, T.; Kodger, T. E.; Capretti, A.; Murray, C. B.; Koenderink, A. F.; Messina, F.; Schall, P., Simultaneous Photonic and Excitonic Coupling in Spherical Quantum Dot Supercrystals. *ACS Nano* **2020,** *14* (10), 13806-13815.
52. Marino, E.; Bharti, H.; Xu, J.; Kagan, C. R.; Murray, C. B., Nanocrystal Superparticles with Whispering-Gallery Modes Tunable through Chemical and Optical Triggers. *Nano Letters* **2022** 22 (12), 4765-4773.
53. Zhu, B.; Guo, G.; Wu, G.; Zhang, Y.; Dong, A.; Hu, J.; Yang, D., Preparation of dual layers N-doped Carbon@Mesoporous Carbon@Fe3O4 nanoparticle superlattice and its application in lithium-ion battery. *Journal of Alloys and Compounds* **2019,** *775*, 776-783.
54. Gu, B.; Su, H.; Chu, X.; Wang, Q.; Huang, H.; He, J.; Wu, T.; Deng, W.; Zhang, H.; Yang, W., Rationally assembled porous carbon superstructures for advanced supercapacitors. *Chemical Engineering Journal* **2019,** *361*, 1296-1303.
55. Yang, Y.; Xiao, J.; Xia, Y.; Xi, X.; Li, T.; Yang, D.; Dong, A., Assembly of CoFe2O4 Nanocrystals into Superparticles with Tunable Porosities for Use as Anode Materials for Lithium-Ion Batteries. *ACS Applied Nano Materials* **2022,** *5* (7), 9698-9705.

56. Yan, W.; Fan, H.; Zhai, Y.; Yang, C.; Ren, P.; Huang, L., Low temperature solution-based synthesis of porous flower-like α-Fe2O3 superstructures and their excellent gas-sensing properties. *Sensors and Actuators B: Chemical* **2011,** *160* (1), 1372-1379.
57. Thomsen, R. P.; Malle, M. G.; Okholm, A. H.; Krishnan, S.; Bohr, S. S. R.; Sørensen, R. S.; Ries, O.; Vogel, S.; Simmel, F. C.; Hatzakis, N. S.; Kjems, J., A large size-selective DNA nanopore with sensing applications. *Nature Communications* **2019,** *10* (1), 5655.
58. Han, D.; Guo, G.; Yan, Y.; Li, T.; Wang, B.; Dong, A., Pomegranate-like, carbon-coated Fe3O4 nanoparticle superparticles for high-performance lithium storage. *Energy Storage Materials* **2018,** *10*, 32-39.
59. Han, W.; Guo, G.; Xia, Y.; Ning, J.; Deng, Y.; Li, W.; Yang, D.; Dong, A., Phase-transfer-assisted confined growth of mesoporous MoS2@graphene van der Waals supraparticles for unprecedented ultrahigh-rate sodium storage. *Journal of Materials Chemistry A* **2021,** *9* (17), 10714-10721.
60. Gopal, S.; Chiappini, C.; Penders, J.; Leonardo, V.; Seong, H.; Rothery, S.; Korchev, Y.; Shevchuk, A.; Stevens, M. M., Porous Silicon Nanoneedles Modulate Endocytosis to Deliver Biological Payloads. *Advanced Materials* **2019,** *31* (12), 1806788.
61. Wei, R.; Gong, X.; Lin, H.; Zhang, K.; Li, A.; Liu, K.; Shan, H.; Chen, X.; Gao, J., Versatile Octapod-Shaped Hollow Porous Manganese(II) Oxide Nanoplatform for Real-Time Visualization of Cargo Delivery. *Nano Letters* **2019,** *19* (8), 5394-5402.
62. Udayabhaskararao, T.; Altantzis, T.; Houben, L.; Coronado-Puchau, M.; Langer, J.; Popovitz-Biro, R.; Liz-Marzán Luis, M.; Vuković, L.; Král, P.; Bals, S.; Klajn, R., Tunable porous nanoallotropes prepared by post-assembly etching of binary nanoparticle superlattices. *Science* **2017,** *358* (6362), 514-518.
63. Cai, Q.; Wang, J.; Jiao, Y.; Li, T.; Xia, Y.; Li, M.; Yang, Y.; Wu, G.; Zou, J.; Hu, J.; Dong, A.; Yang, D., All-Graphitic Multilaminate Mesoporous Membranes by Interlayer-Confined Molecular Assembly. *Small* **2021,** *17* (24), 2101173.
64. Håkonsen, V.; Singh, G.; He, J.; Zhang, Z., Focused ion beam milling of self-assembled magnetic superstructures: an approach to fabricate nanoporous materials with tunable porosity. *Materials Horizons* **2018,** *5* (6), 1211-1218.
65. Wooh, S.; Huesmann, H.; Tahir, M. N.; Paven, M.; Wichmann, K.; Vollmer, D.; Tremel, W.; Papadopoulos, P.; Butt, H.-J., Synthesis of Mesoporous Supraparticles on Superamphiphobic Surfaces. *Advanced Materials* **2015,** *27* (45), 7338-7343.
66. Liu, W.; Kappl, M.; Butt, H.-J., Tuning the Porosity of Supraparticles. *ACS Nano* **2019,** *13* (12), 13949-13956.
67. Elbert, K. C.; Vo, T.; Oh, D.; Bharti, H.; Glotzer, S. C.; Murray, C. B., Evaporation-Driven Coassembly of Hierarchical, Multicomponent Networks. *ACS Nano* **2022,** *16* (3), 4508-4516.
68. Yang, M.; Cao, K.; Sui, L.; Qi, Y.; Zhu, J.; Waas, A.; Arruda, E. M.; Kieffer, J.; Thouless, M. D.; Kotov, N. A., Dispersions of Aramid Nanofibers: A New Nanoscale Building Block. *ACS Nano* **2011,** *5* (9), 6945-6954.
69. Wang, M.; Vecchio, D.; Wang, C.; Emre, A.; Xiao, X.; Jiang, Z.; Bogdan, P.; Huang, Y.; Kotov Nicholas, A., Biomorphic structural batteries for robotics. *Science Robotics* **2020,** *5* (45), eaba1912.
70. Podsiadlo, P.; Sui, L.; Elkasabi, Y.; Burgardt, P.; Lee, J.; Miryala, A.; Kusumaatmaja, W.; Carman, M. R.; Shtein, M.; Kieffer, J.; Lahann, J.; Kotov, N. A., Layer-by-Layer Assembled Films of Cellulose Nanowires with Antireflective Properties. *Langmuir* **2007,** *23* (15), 7901-7906.
71. Parente, M.; van Helvert, M.; Hamans, R. F.; Verbroekken, R.; Sinha, R.; Bieberle-Hütter, A.; Baldi, A., Simple and Fast High-Yield Synthesis of Silver Nanowires. *Nano Letters* **2020,** *20* (8), 5759-5764.
72. Tang, L.; Vo, T.; Fan, X.; Vecchio, D.; Ma, T.; Lu, J.; Hou, H.; Glotzer, S. C.; Kotov, N. A., Self-Assembly Mechanism of Complex Corrugated Particles. *Journal of the American Chemical Society* **2021,** *143* (47), 19655-19667.
73. Xu, Z.; Zhuang, X.; Yang, C.; Cao, J.; Yao, Z.; Tang, Y.; Jiang, J.; Wu, D.; Feng, X., Nitrogen-Doped Porous Carbon Superstructures Derived from Hierarchical Assembly of Polyimide Nanosheets. *Advanced Materials* **2016,** *28* (10), 1981-1987.
74. Park, J.; An, K.; Hwang, Y.; Park, J.-G.; Noh, H.-J.; Kim, J.-Y.; Park, J.-H.; Hwang, N.-M.; Hyeon, T., Ultra-large-scale syntheses of monodisperse nanocrystals. *Nature Materials* **2004,** *3* (12), 891-895.
75. Hanifi David, A.; Bronstein Noah, D.; Koscher Brent, A.; Nett, Z.; Swabeck Joseph, K.; Takano, K.; Schwartzberg Adam, M.; Maserati, L.; Vandewal, K.; van de Burgt, Y.; Salleo, A.; Alivisatos, A. P., Redefining near-unity luminescence in quantum dots with photothermal threshold quantum yield. *Science* **2019,** *363* (6432), 1199-1202.
76. Walton, W. H., Feret's Statistical Diameter as a Measure of Particle Size. *Nature* **1948,** *162* (4113), 329-330.
77. Abbas, A. S.; Vargo, E.; Jamali, V.; Ercius, P.; Pieters, P. F.; Brinn, R. M.; Ben-Moshe, A.; Cho, M. G.; Xu, T.; Alivisatos, A. P., Observation of an Orientational Glass in a Superlattice of Elliptically-Faceted CdSe Nanocrystals. *ACS Nano* **2022,** 16, 6, 9339–9347.
78. Metropolis, N.; Rosenbluth, A. W.; Rosenbluth, M. N.; Teller, A. H.; Teller, E., Equation of State Calculations by Fast Computing Machines. *The Journal of Chemical Physics* **2004,** *21* (6), 1087-1092.
79. Ramasubramani, V.; Dice, B. D.; Harper, E. S.; Spellings, M. P.; Anderson, J. A.; Glotzer, S. C., freud: A software suite for high throughput analysis of particle simulation data. *Computer Physics Communications* **2020,** *254*, 107275.
80. Marino, E.; Keller, A. W.; An, D.; van Dongen, S.; Kodger, T. E.; MacArthur, K. E.; Heggen, M.; Kagan, C. R.; Murray, C. B.; Schall, P., Favoring the Growth of High-Quality, Three-Dimensional Supercrystals of Nanocrystals. *The Journal of Physical Chemistry C* **2020,** *124* (20), 11256-11264.
81. Tang, Y.; Gomez, L.; Lesage, A.; Marino, E.; Kodger, T. E.; Meijer, J.-M.; Kolpakov, P.; Meng, J.; Zheng, K.; Gregorkiewicz, T.; Schall, P., Highly Stable Perovskite Supercrystals via Oil-in-Oil Templating. *Nano Letters* **2020,** *20* (8), 5997-6004.
82. Montanarella, F.; Geuchies, J. J.; Dasgupta, T.; Prins, P. T.; van Overbeek, C.; Dattani, R.; Baesjou, P.; Dijkstra, M.; Petukhov, A. V.; van Blaaderen, A.; Vanmaekelbergh, D., Crystallization of Nanocrystals in Spherical Confinement Probed by in Situ X-ray Scattering. *Nano Letters* **2018,** *18* (6), 3675-3681.
83. Kister, T.; Mravlak, M.; Schilling, T.; Kraus, T., Pressure-controlled formation of crystalline, Janus, and core–shell supraparticles. *Nanoscale* **2016,** *8* (27), 13377-13384.
84. Wang, D.; Dasgupta, T.; van der Wee, E. B.; Zanaga, D.; Altantzis, T.; Wu, Y.; Coli, G. M.; Murray, C. B.; Bals, S.; Dijkstra, M.; van Blaaderen, A., Binary icosahedral clusters of hard spheres in spherical confinement. *Nature Physics* **2021,** *17* (1), 128-134.
85. Wang, D.; van der Wee, E. B.; Zanaga, D.; Altantzis, T.; Wu, Y.; Dasgupta, T.; Dijkstra, M.; Murray, C. B.; Bals, S.; van Blaaderen, A., Quantitative 3D real-space analysis of Laves phase supraparticles. *Nature Communications* **2021,** *12* (1), 3980.
86. Wang, D.; Hermes, M.; Kotni, R.; Wu, Y.; Tasios, N.; Liu, Y.; de Nijs, B.; van der Wee, E. B.; Murray, C. B.; Dijkstra, M.; van Blaaderen, A., Interplay between spherical confinement and particle shape on the self-assembly of rounded cubes. *Nature Communications* **2018,** *9* (1), 2228.
87. Yang, Y.; Wang, B.; Shen, X.; Yao, L.; Wang, L.; Chen, X.; Xie, S.; Li, T.; Hu, J.; Yang, D.; Dong, A., Scalable Assembly of Crystalline Binary Nanocrystal Superparticles and Their Enhanced Magnetic and Electrochemical Properties. *Journal of the American Chemical Society* **2018,** *140* (44), 15038-15047.

88. Wang, P.-p.; Qiao, Q.; Zhu, Y.; Ouyang, M., Colloidal Binary Supracrystals with Tunable Structural Lattices. *Journal of the American Chemical Society* **2018,** *140* (29), 9095-9098.
89. Tian, Y.; Lhermitte, J. R.; Bai, L.; Vo, T.; Xin, H. L.; Li, H.; Li, R.; Fukuto, M.; Yager, K. G.; Kahn, J. S.; Xiong, Y.; Minevich, B.; Kumar, S. K.; Gang, O., Ordered three-dimensional nanomaterials using DNA-prescribed and valence-controlled material voxels. *Nature Materials* **2020,** *19* (7), 789-796.
90. Chen, O.; Riedemann, L.; Etoc, F.; Herrmann, H.; Coppey, M.; Barch, M.; Farrar, C. T.; Zhao, J.; Bruns, O. T.; Wei, H.; Guo, P.; Cui, J.; Jensen, R.; Chen, Y.; Harris, D. K.; Cordero, J. M.; Wang, Z.; Jasanoff, A.; Fukumura, D.; Reimer, R.; Dahan, M.; Jain, R. K.; Bawendi, M. G., Magneto-fluorescent core-shell supernanoparticles. *Nature Communications* **2014,** *5* (1), 5093.
91. Mandal, S. K.; Lequeux, N.; Rotenberg, B.; Tramier, M.; Fattaccioli, J.; Bibette, J.; Dubertret, B., Encapsulation of Magnetic and Fluorescent Nanoparticles in Emulsion Droplets. *Langmuir* **2005,** *21* (9), 4175-4179.
92. Turro, N. J.; Lakshminarasimhan, P. H.; Jockusch, S.; O'Brien, S. P.; Grancharov, S. G.; Redl, F. X., Spectroscopic Probe of the Surface of Iron Oxide Nanocrystals. *Nano Letters* **2002,** *2* (4), 325-328.
93. Kim, B.-S.; Taton, T. A., Multicomponent Nanoparticles via Self-Assembly with Cross-Linked Block Copolymer Surfactants. *Langmuir* **2007,** *23* (4), 2198-2202.
94. Förster, T., Zwischenmolekulare Energiewanderung und Fluoreszenz. *Annalen der Physik* **1948,** *437* (1-2), 55-75.
95. Ouzit, Z.; Baillard, G.; Liu, J.; Wagnon, B.; Guillemeney, L.; Abécassis, B.; Coolen, L., Luminescence Dynamics of Single Self-Assembled Chains of Förster (FRET)-Coupled CdSe Nanoplatelets. *The Journal of Physical Chemistry Letters* **2023**, 6209-6216.
96. Lakowicz, J. R., Chapter 13: Energy Transfer. In *Principles of Fluorescence Spectroscopy*, Lakowicz, J. R., Ed. Springer US: Boston, MA, 2006; pp 443-475.
97. Rosen, D. J.; Yang, S.; Marino, E.; Jiang, Z.; Murray, C. B., In Situ EXAFS-Based Nanothermometry of Heterodimer Nanocrystals under Induction Heating. *The Journal of Physical Chemistry C* **2022,** *126* (7), 3623-3634.
98. Brown, J. W.; Henderson, B. L.; Kiesz, M. D.; Whalley, A. C.; Morris, W.; Grunder, S.; Deng, H.; Furukawa, H.; Zink, J. I.; Stoddart, J. F.; Yaghi, O. M., Photophysical pore control in an azobenzene-containing metal–organic framework. *Chemical Science* **2013,** *4* (7), 2858-2864.
99. Epley, C. C.; Roth, K. L.; Lin, S.; Ahrenholtz, S. R.; Grove, T. Z.; Morris, A. J., Cargo delivery on demand from photodegradable MOF nano-cages. *Dalton Transactions* **2017,** *46* (15), 4917-4922.
100. Wenderoth, S.; Müssig, S.; Prieschl, J.; Genin, E.; Heuzé, K.; Fidler, F.; Haddad, D.; Wintzheimer, S.; Mandel, K., Optically Sensitive and Magnetically Identifiable Supraparticles as Indicators of Surface Abrasion. *Nano Letters* **2022,** *22* (7), 2762-2768.
101. Liu, J.; Xiao, M.; Li, C.; Li, H.; Wu, Z.; Zhu, Q.; Tang, R.; Xu, A. B.; He, L., Rugby-ball-like photonic crystal supraparticles with non-close-packed structures and multiple magneto-optical responses. *Journal of Materials Chemistry C* **2019,** *7* (47), 15042-15048.
102. Maqbool, Q.; Jung, A.; Won, S.; Cho, J.; Son, J. G.; Yeom, B., Chiral Magneto-Optical Properties of Supra-Assembled Fe3O4 Nanoparticles. *ACS Applied Materials & Interfaces* **2021,** *13* (45), 54301-54307.
103. Müssig, S.; Reichstein, J.; Miller, F.; Mandel, K., Colorful Luminescent Magnetic Supraparticles: Expanding the Applicability, Information Capacity, and Security of Micrometer-Scaled Identification Taggants by Dual-Spectral Encoding. *Small* **2022,** *18* (13), 2107511.

TOC graphic